

Statistical Bias in the Hubble Constant and Mass Power Law Slope for Mock Strong Lenses

Dilys Ruan,¹★ Charles R. Keeton¹

¹ *Department of Physics and Astronomy, Rutgers University, Piscataway, NJ 08854, USA*

Accepted XXX. Received YYY; in original form ZZZ

ABSTRACT

Strong gravitational lensing offers constraints on the Hubble constant that are independent of other methods. However, those constraints are subject to uncertainties in lens models. Previous studies suggest that using an elliptical power law + external shear (EPL+XS) for the lensing galaxy can yield results that are precise but inaccurate. We examine such models by generating and fitting mock lenses which produces multiple images of a background quasar-like point source. Despite using the same model for input and output, we find statistical bias in the Hubble constant on the order of 3% to 5%, depending on whether the elliptical lenses have noise or not. The phase space distribution has a ‘flared’ shape that causes the mass power law slope to be underestimated and the Hubble constant to be overestimated. The bias varies with image configuration, which we quantify through annulus length between images with the first and second time delays ($\Delta r_{1,2}$). The statistical bias is worse for configurations that have narrow annuli (e.g., symmetric cross configurations). Assuming a source at redshift 2.0 and an EPL+XS lens at redshift 0.3, we find that the bias can be reduced, but not eliminated, if we limit the sample to systems with annulus lengths $\Delta r_{1,2} \gtrsim 0.3$ arcsec. As lens samples grow, it may be helpful to prioritize this range of image configurations for follow-up observation and analysis.

Key words: gravitational lensing: strong – (cosmology:) cosmological parameters – galaxies: general

1 INTRODUCTION

The Hubble tension describes a 4–6 σ discrepancy between ‘local’ and ‘distant’ measurements of the current expansion rate of the Universe, or the Hubble constant (H_0). Local measurements such as those from Cepheid stars + Type Ia supernovae (Riess et al. 2019; Freedman 2021a), Tip of the Red Giant Branch stars + Type Ia supernovae (Freedman et al. 2019; Freedman 2021b), gravitational lensing (Wong et al. 2020; Birrer et al. 2020), and masers (Reid et al. 2019; Pesce et al. 2020) tend to find a higher value of H_0 than the distant measurements made with the cosmic microwave background (CMB) and baryon acoustic oscillations (Planck Collaboration et al. 2020a,b). The tension could be interpreted as evidence for a cosmological model that deviates from fiducial Λ CDM (Knox & Millea 2020; Di Valentino et al. 2021), but before drawing such a conclusion it is crucial to assess possible sources of errors with each measurement. In this study we examine constraints on H_0 from gravitational lensing.

Gravitational lensing provides a local measurement of H_0 that is independent of the distance ladder. In strong lensing, the gravitational deflection of light creates multiple images of a background source, and any variability in the source will be delayed between images because the light rays travel different paths. Often the background source is a quasar or supernova, while the foreground lens is a massive elliptical galaxy. The COSMOGRAIL team has undertaken long-term monitoring to measure lensing time delays (even

accounting for additional variability produced by microlensing; Bonvin et al. 2018a; Millon et al. 2020b), and upcoming surveys such as the Rubin Observatory’s Legacy Survey of Space and Time (LSST) should significantly increase the sample (LSST Dark Energy Science Collaboration 2012; Oguri & Marshall 2010).

Time delays must be interpreted in the context of a lens model, and this is where statistical and systematic errors may arise. Most lens models are categorized by their treatment of radial and angular components in the lens potential. Objects in the environment of the main lens galaxy or along the line-of-sight also contribute to the lens potential, and these effects are often treated with a multipole expansion. A common simplification in lens modelling is to fit the main lens galaxy with an elliptical power law (EPL) and then add external shear (XS) to account for environmental and line-of-sight effects. However, there are some exact or approximate degeneracies in lens models, such as the mass sheet degeneracy and radial profile degeneracy (Falco et al. 1985; Saha 2000; Kochanek 2002). Stellar velocity dispersions provide a lensing-independent way to break these degeneracies and constrain the density profile (e.g., Romanowsky & Kochanek 1999; Treu & Koopmans 2002; Wong et al. 2020; Birrer et al. 2020). An isothermal elliptical model appears to be fairly accurate near the Einstein radius where images form, but this is not necessarily true at smaller or larger radii (van de Ven et al. 2009; Cappellari et al. 2013).

After analyzing six lens systems from COSMOGRAIL, the H0LiCOW team measured $H_0 = 73.3^{+1.7}_{-1.8}$ km s^{−1} Mpc^{−1} (Wong et al. 2020). The TDCOSMO team used hierarchical Bayesian analysis on these six lenses plus one more system to obtain $H_0 = 74.5^{+5.6}_{-6.1}$

★ E-mail: druan@physics.rutgers.edu

km s⁻¹ Mpc⁻¹ (Birrer et al. 2020). To improve the measurement, they included another 33 systems from SLACS, nine of which have resolved stellar kinematics. Assuming that galaxies from SLACS and TDCOSMO are drawn from the same parent population, the team used joint Bayesian analysis to find $H_0 = 67.4^{+4.1}_{-3.2}$ km s⁻¹ Mpc⁻¹ – a 5% precision measurement that is closer to the H_0 value measured from the CMB.

The sample of strong lenses will grow by orders of magnitude with current and upcoming surveys. STRIDES is expected to find about 250 lens candidates in Stage 2 (Treu et al. 2018), and has recently discovered 30 new lenses (Schmidt et al. 2023). The Rubin Observatory’s LSST should discover more than 8000 lenses through high-cadence, 10-year observations of 18000 deg² of the sky (LSST Dark Energy Science Collaboration 2012; Oguri & Marshall 2010). Euclid, Rubin, the Square Kilometre Array, and JWST will collectively provide deep, multi-wavelength observations of $\sim 10^5$ lenses (McKean et al. 2015; Weiner et al. 2020). As larger samples improve the statistical precision, it is ever more important to understand systematic uncertainties for competitive H_0 measurements (Ding et al. 2021).

Multiple studies have examined bias in H_0 caused by mismatches between true and fitted mass distributions. Many studies have generated lenses with a composite model (i.e., baryons + dark matter) with XS, and fitted the time delay data with an EPL+XS. Schneider & Sluse (2013) fitted each lens with its true stellar velocity dispersion. Although best-fit models reproduced the data well, H_0 bias was $\sim 20\%$. Gomer & Williams (2020) similarly found that kinematic constraints from a Jeans analysis led to H_0 bias ranging from 0-23%, depending on the image radius. Kochanek (2020) noted that if few-parameter mass distributions (like the EPL+XS) are assumed, it is possible to obtain results that are precise but inaccurate. In contrast to this result, Millon et al. (2020a) explored systematic uncertainties in the TDCOSMO analysis and found that composite and EPL models with XS gave statistically consistent results.

In this study, we identify a statistical bias that arises even if the same mass distribution is used to generate and fit mock lens galaxies. We consider three classes of models: a circular power law that offers some insightful analytic results, as well as circular and elliptical power laws with external shear. Section 2 describes our methodology, Section 3 presents our results for the three model classes, and Section 4 summarizes our conclusions. Appendix A examines some technical aspects of our modelling analysis. We assume a flat Λ CDM cosmology, with $\Omega_m = 0.315$, $\Omega_\Lambda = 0.685$, and $h = 0.7$ where $H_0 = 100h$ km s⁻¹ Mpc⁻¹. Code is available on GitHub to demonstrate how we performed the analysis¹.

2 METHODS

2.1 Time Delay Cosmography & Lens Model

We summarize key aspects of time delay cosmography and refer the reader to comprehensive reviews for more details on this topic (e.g., Treu & Marshall 2016; Shajib et al. 2022) and gravitational lensing more broadly (e.g., Congdon & Keeton 2018). According to Fermat’s Principle, light rays follow paths that correspond to stationary points of the time delay surface

$$\tau(\theta|\beta) = \frac{D_{\Delta t}}{c} \Phi(\theta|\beta), \quad (1)$$

where θ is the angular position in the image plane, β is the intrinsic angular position of the source, and the time delay distance $D_{\Delta t}$ depends on the lens and source redshifts through cosmological angular diameter distances,

$$D_{\Delta t} = (1 + z_l) \frac{D(z_l) D(z_s)}{D(z_l, z_s)}. \quad (2)$$

The Fermat Potential is

$$\Phi(\theta, \beta) = \frac{1}{2} (\theta - \beta)^2 - \psi(\theta), \quad (3)$$

where $\psi(\theta)$ is the projected gravitational potential of the lens. The first term in Φ accounts for the travel time due to the geometric path, while the second term in Φ accounts for relativistic time dilation. The basic idea of time delay cosmography is to measure the time delay $\Delta\tau_{AB}$ between two images, use a lens model to compute the difference in Fermat potential $\Delta\Phi_{AB}$, and then use Equation (1) to solve for the time delay distance and constrain H_0 .

The source and image positions are related by the lens equation

$$\beta = \theta - \alpha(\theta), \quad (4)$$

where the deflection angle $\alpha = \nabla\psi(\theta)$ is the gradient of the lens potential. The lens potential is determined by the surface mass density through the Poisson equation

$$\nabla^2\psi(\theta) = 2\kappa(\theta) = \frac{2\Sigma(\theta)}{\Sigma_{crit}}, \quad (5)$$

where the convergence κ is the surface mass density scaled by the critical density for lensing,

$$\Sigma_{crit} = \frac{c^2}{4\pi G} \frac{D(z_s)}{D(z_l)D(z_l, z_s)}. \quad (6)$$

The lensing magnification is given by $\mu = \det A$ where the amplification tensor is $A = \partial\theta/\partial\beta = (\partial\beta/\partial\theta)^{-1}$.

We consider a power law density profile. For circular symmetry, the lens potential, deflection angle, and convergence have the respective forms

$$\psi(r) = \frac{R_E^{2-\eta}}{\eta} r^\eta, \quad (7)$$

$$\alpha(r) = R_E^{2-\eta} r^{\eta-1}, \quad (8)$$

$$\kappa(r) = \frac{\eta}{2} R_E^{2-\eta} r^{\eta-2}. \quad (9)$$

Here R_E is the Einstein radius and η is the mass power law slope. An isothermal profile has $\eta = 1$. It can be convenient to express the normalization through a simple multiplicative factor²

$$b = R_E^{2-\eta}, \quad (10)$$

and we will use this form for the majority of our analysis. We can obtain an elliptical mass distribution by replacing r in the convergence with the elliptical radius $\sqrt{q^2x^2 + y^2}$, where $0 < q \leq 1$ is the ratio of the short to long axes. In models we use the quasi-Cartesian components that are expressed in terms of the ellipticity $e = 1 - q$ and orientation angle θ_e as $e_c = e \cos 2\theta_e$ and $e_s = e \sin 2\theta_e$. We implement expressions for the potential, deflection, and magnification of the elliptical power law model from Tessore & Metcalf (2015, 2016). In some cases we also consider an external shear, whose lens potential has the form

$$\psi_{XS}(\theta) = \frac{1}{2} \theta \cdot \Gamma \cdot \theta \quad \text{where} \quad \Gamma = \begin{bmatrix} \gamma_c & \gamma_s \\ \gamma_s & -\gamma_c \end{bmatrix}. \quad (11)$$

¹ <https://github.com/dilysruan/paper-ruan-keeton-2023>

² The goodness of fit χ^2_{pos} in Equation (12) is quadratic in b .

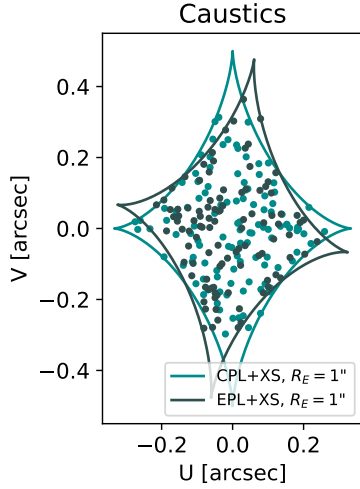


Figure 1. Caustic curves for the CPL+XS (teal) and EPL+XS (dark teal) lenses. There are 100 sources (markers) at different positions within the caustic curves for each mass distribution.

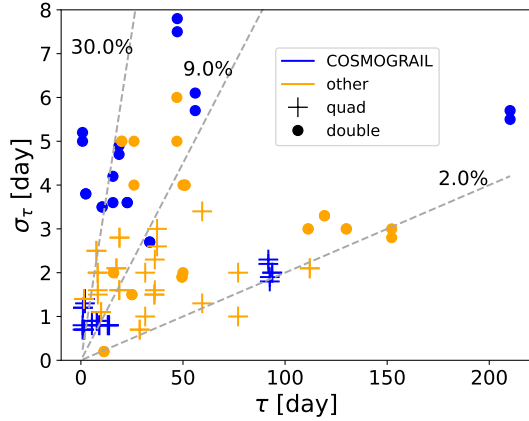


Figure 2. The relative time delay values (τ) and uncertainties (σ_τ) for observed lens systems listed in Table 3 of Millon et al. (2020b). The dashed lines indicate certain percentage errors.

Here γ_c and γ_s are quasi-Cartesian components of shear, which are related to the shear amplitude γ and direction θ_γ as $\gamma_c = \gamma \cos 2\theta_\gamma$ and $\gamma_s = \gamma \sin 2\theta_\gamma$.

2.2 Generating Mock Data

We use `pygravlens`³, a python version of the gravitational lensing code `gravlens` (Keeton 2011). We choose as our fiducial model an isothermal mass distribution ($\eta = 1$) with a lens galaxy at $z_l = 0.3$ and a source quasar at $z_s = 2.0$. We create circular models with and without shear, and an elliptical model with shear. The fiducial parameter values are given in Table 1. For each mass distribution, we choose random source positions from a uniform distribution that is centered on the origin and spans the caustic curve. Both the CPL+XS and EPL+XS caustics span ~ 0.8 arcsec along the long axis, as shown in Figure 1.

³ <https://github.com/chuckkeeton/pygravlens>

The image position uncertainties are 0.003 arcsec, and flux uncertainties are 5%. To identify reasonable values for the time delay uncertainties, Figure 2 shows observed time delays and uncertainties from Table 3 in Millon et al. (2020b), which includes values from the COSMOGRAIL study and previous studies (Biggs & Browne 2018; Courbin et al. 2018; Hainline et al. 2013; Jakobsson et al. 2005; Rathna Kumar et al. 2013; Poindexter et al. 2007; Bonvin et al. 2018b; Eulaers et al. 2013; Goicoechea & Shalyapin 2016; Akhunov et al. 2017; Patnaik & Narasimha 2001; Shalyapin & Goicoechea 2019; Burud et al. 2002, 2000; Fassnacht et al. 2002; Vuissoz et al. 2007; Lovell et al. 1998; Bonvin et al. 2019). Time delays can range from a few days to 100 days or more, and there is no obvious trend in terms of percentage uncertainty. We therefore choose to use the median values of the uncertainties, which are 3.0 days for doubly-imaged systems and 2.0 days for quadruply-imaged systems. We adopt these as the time delay uncertainties for our mock lenses. Statistical noise is only added to the mock data in Section 3.5.

2.3 Fitting Models

When fitting models, we can impose constraints from image positions, flux ratios, and time delays through the following goodness-of-fit functions:

$$\chi^2_{pos} = \sum_i [\beta + \alpha_i - \theta_i]^T A_i^T C_i^{-1} A_i [\beta + \alpha_i - \theta_i], \quad (12)$$

$$\chi^2_{flux} = \sum_i \frac{(\mu_i f_{src} - f_{obs,i})^2}{\sigma_{f,i}^2}, \quad (13)$$

$$\chi^2_{idel} = \sum_i \frac{(\Delta t_{mod,i} - \Delta t_{obs,i})^2}{\sigma_{t,i}^2}. \quad (14)$$

Here the observed quantities are the image positions θ_i and covariance matrices C_i for the position uncertainties, the fluxes $f_{obs,i}$ and their uncertainties $\sigma_{f,i}$, and the time delays $\Delta t_{obs,i}$ and their uncertainties $\sigma_{t,i}$. The model quantities are the source position β and source flux f_{src} , as well as parameters for the mass model (R_E or b and η , along with ellipticity and/or shear if they are used). The Hubble parameter h enters the predicted time delays through the scaling $\Delta t_{mod} \propto h^{-1}$.

In some cases we also impose a prior on the power law slope through

$$\chi^2_{PL} = \frac{(\eta_{mod} - \eta_{obs})^2}{\sigma_{PL}^2}. \quad (15)$$

This prior is meant to mimic adding constraints from stellar kinematics. Following constraints on the power law slope given in Table 2 of Birrer et al. (2020), we adopt $\eta_{obs} = 1.0$ and $\sigma_{PL} = 0.1$.

We constrain the model parameters using Bayesian inference with the likelihood function $L \propto e^{-\chi^2/2}$. We work analytically in certain cases described below. More generally, we sample the Bayesian posterior using MCMC methods implemented in the code `emcee` (Foreman-Mackey et al. 2013). We assume flat priors on the parameters (except for η as noted above). In some cases the parameters are well constrained such that we do not need to impose explicit bounds. However, other cases are not well constrained, so we impose the bounds $\eta \in (0.5, 1.5)$ and $h \in (0, 1.2)$ in order to avoid values that are implausible or unphysical. MCMC runs for the CPL+XS and EPL+XS systems use 100 walkers, 8000 burn-in steps, and 8000 main steps.

There are several choices that must be made in the modelling process. Nuisance parameters can be fully marginalized or merely

Case	R_E	e_c	e_s	γ_c	γ_s	η	h	σ_τ [days]
Doubly-Imaged CPL	1.0	0	0	0	0	1.0	0.7	3.0
Quadruply-Imaged CPL+XS	1.0	0	0	0.2	0	1.0	0.7	2.0, 4.0
Quadruply-Imaged EPL+XS	1.0	0.15	0.15	0.22	0	1.0	0.7	2.0

Table 1. Input values for the various lens model parameters. R_E is the Einstein radius, e_c and e_s are quasi-Cartesian components of ellipticity, and γ_c and γ_s are the corresponding quasi-Cartesian components of external shear. The input Λ CDM cosmology has $\Omega_m = 0.315$, $\Omega_\Lambda = 0.685$, and $h = 0.7$.

optimized (i.e., set to their best-fit values). For parameters that are quadratic in χ^2 , the optimal values can be computed analytically to reduce computational effort. Statistically, however, marginalization is preferred. As noted above, the mass model can be specified using either the Einstein radius R_E or the mass parameter b . Our fiducial results use marginalization and the ‘b mode’ normalization. Flux ratio constraints are used for the CPL case in order to break the degeneracy for doubly-imaged systems. We do not apply them for the quadruply-imaged CPL+XS or EPL+XS cases since flux ratios can be affected by microlensing and are not generally used as constraints in time delay studies (Chen et al. 2019; Rusu et al. 2020). Appendix A compares other modelling choices and shows that they do not significantly change our results.

3 RESULTS & DISCUSSION

3.1 Doubly-Imaged Circular Power Law

We begin with the simple case of a circular lens (with no external shear) so key results can be understood analytically. A circular lens can produce two images on opposite sides of the origin; let their distances from the origin be $\theta_A > \theta_B > 0$. Then the lens equations for the two images can be written as

$$\begin{aligned} \beta &= \theta_A - b \theta_A^{\eta-1} \\ -\beta &= \theta_B - b \theta_B^{\eta-1} \end{aligned} \quad (16)$$

The equation for image B has a minus sign on the left because the image lies on the opposite side of the lens from the source. These two equations can be solved for b and β ,

$$b = \frac{\theta_A + \theta_B}{\theta_A^{\eta-1} + \theta_B^{\eta-1}} \quad \text{and} \quad \beta = \frac{\theta_A \theta_B^{\eta-1} - \theta_B \theta_A^{\eta-1}}{\theta_A^{\eta-1} + \theta_B^{\eta-1}} \quad (17)$$

which means the image positions can be reproduced by *any* value of the power law slope η . Thus, flux constraints are needed to break the radial profile degeneracy. Using the analytic solutions for b and β ensures that the goodness of fit for the image positions is $\chi_{pos}^2 = 0$, so the overall goodness of fit in this analysis is $\chi^2 = \chi_{flux}^2 + \chi_{del}^2$.

We consider two mock systems with different source locations, as shown in Figure 3. The source for Mock 1 is closer to the origin, so the two images are closer to the Einstein radius and have higher magnifications. The annulus spanned by the images is narrower for Mock 1 and wider for Mock 2.

Since we solve for b and β using Equation (17), and we optimize the intrinsic flux of the source (which can also be done analytically since χ_{flux}^2 is quadratic in f_{src}), the only parameters that need to be explored by MCMC are η and h . Figure 4 shows posterior distributions for both Mock 1 and Mock 2. The posterior for Mock 2 is quite narrow and encloses the input values, with medians of $\eta = 0.999^{+0.033}_{-0.034}$ and $h = 0.707^{+0.048}_{-0.043}$. By contrast, the posterior for Mock 1 is much broader. Although it encloses the input values,

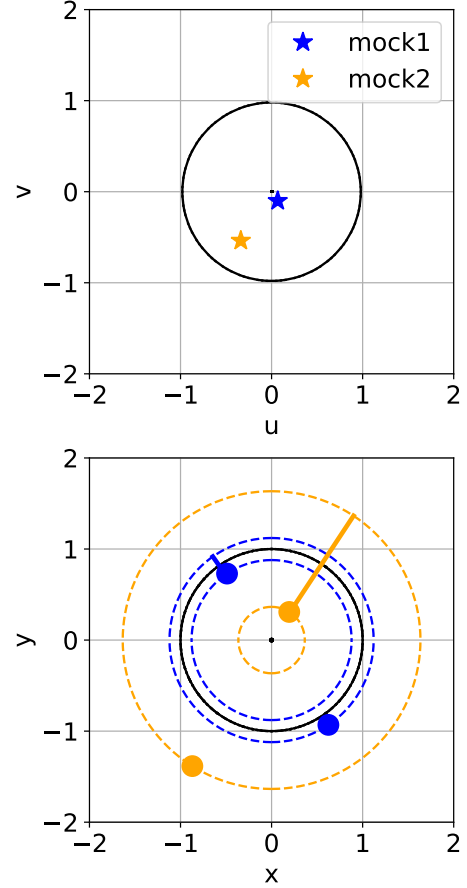


Figure 3. The source plane (*top*) and image plane (*bottom*) for the doubly-imaged circular lens systems CPL Mock 1 (blue markers) and CPL Mock 2 (orange markers). The caustic and critical curves are shown with the solid black lines. Mock 1 has a source closer to the origin, which results in images that are closer together in radii, while the images from Mock 2 are more spread out. The annulus made by each lens system are shown with the dashed lines. The solid colored line represents the annulus size between images for each lens system. Axes are labeled in units of arcsec.

the medians are significantly biased with $\eta = 0.939^{+0.271}_{-0.276}$ and $h = 0.905^{+0.477}_{-0.310}$.

The difference in posteriors can be understood using Figure 5, which shows the magnification ratio of the images as a function of the power law slope η . For Mock 2, the curve is quite steep because the image radii are different; as a result, only a narrow range of η values can produce a magnification ratio that is consistent with the ‘observed’ value. For Mock 1, by contrast, the curve of magnification ratio vs. η is shallower because the image radii are similar; in this case, the range of η values that are consistent with the data is much broader. In other words, the narrow image annulus in Mock 1 provides

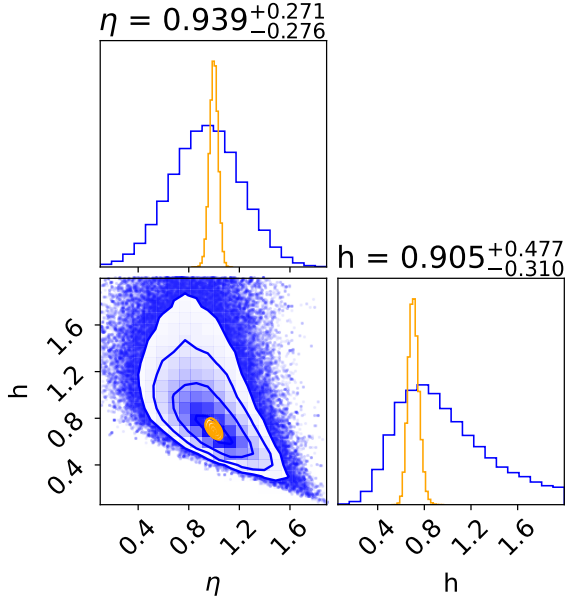


Figure 4. MCMC results for CPL Mock 1 (blue) and Mock 2 (orange). Column titles give the median values and 68% confidence intervals for Mock 1. For Mock 2, the corresponding results are $\eta = 0.999^{+0.033}_{-0.034}$ and $h = 0.707^{+0.048}_{-0.043}$.

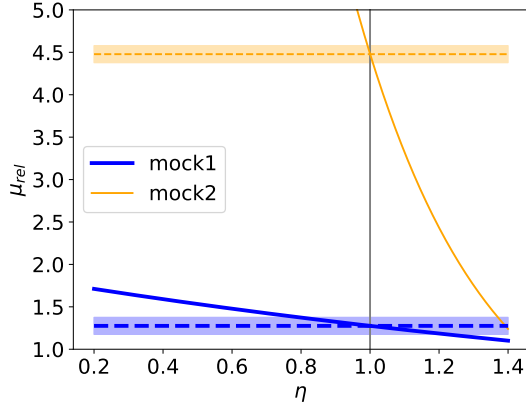


Figure 5. The solid curves show the predicted image magnification ratio as a function of the power law slope for Mock 1 (thicker blue) and Mock 2 (orange). The dashed lines and shaded regions represent the ‘observed’ magnification ratios and uncertainties for the two systems. The grey vertical line indicates the input power law slope, $\eta = 1$.

worse sampling of the mass profile, leading to larger uncertainties in the lens model.

It is important to note that the *peak* of each posterior distribution corresponds to the input values of $\eta = 1$ and $h = 0.7$, because those values yield a perfect fit with $\chi^2 = 0$. However, the *median* values of the marginalized distributions can be shifted away from the input values because of the shape of the posterior distribution. Figure 4 shows that the joint posterior $p(\eta, h)$ exhibits a ‘flared’ shape: it is narrower in the lower right and becomes broader in the upper left. This effect can be understood analytically as follows. For each value of η , we can solve for b and β using Equation (17) and thus predict the model time delay Δt_{mod} . We can then compute the conditional probability distribution $p(h|\eta) \propto e^{-\chi^2_{idel}}$ using Equation

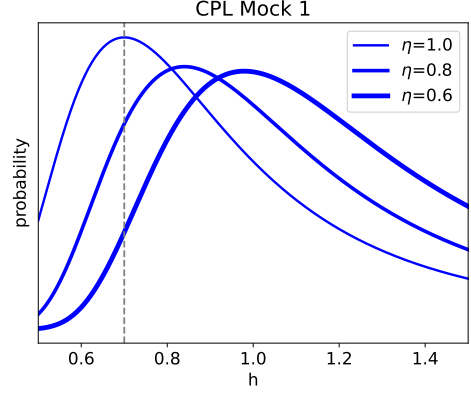


Figure 6. Analytic results for the conditional probability distribution $p(h|\eta)$ for CPL Mock 1 as the power law slope η varies. As η decreases, the curve not only shifts but also broadens. The grey dashed line shows the input truth $h = 0.7$.

(14). Figure 6 shows the resulting analytic curves for Mock 1. The scaling $\Delta t_{mod} \propto h^{-1}$ means that h follows a reciprocal Gaussian distribution. As η decreases, the $p(h|\eta)$ curve not only shifts but also broadens. The net effect is that there is more phase space at lower values of η and higher values of h . Because of this statistical effect, the power law slope η tends to be underestimated and h tends to be overestimated. This statistical bias is larger in systems like Mock 1 that are less constrained and thus have larger model uncertainties.

3.2 Quadruply-Imaged Circular Power Law + External Shear

We expand the analysis to a more realistic model by including external shear. In this case the model can produce quad lenses, and we focus on them because having four images provides more constraints on the lens model. We pick random sources to produce 100 mock quad lenses. For each system, there are seven free parameters: two source position coordinates, Einstein radius, two components of shear, power law slope, and h .

Figure B1 shows the full MCMC results for CPL+XS Mock 77, a fold configuration. Here we use constraints from image positions and time delays, so the goodness of fit is $\chi^2 = \chi^2_{pos} + \chi^2_{idel}$. The constraints from Mock 77 are strong enough to produce a single-peaked posterior distribution that is ‘compact’ in the sense of being contained within the prior range, and the fitted value for each parameter is consistent with the input truth. Even so, the (η, h) posterior shows some degree of ‘flaring’ like we saw in the CPL case, leading to some bias in the median values.

Below we will see that EPL+XS lens models have more freedom and often need priors on the power law slope in order to be well constrained. To enable a fair comparison between CPL+XS and EPL+XS cases, we rerun the current circular models with the priors on η such that the goodness of fit is now $\chi^2 = \chi^2_{pos} + \chi^2_{idel} + \chi^2_{PL}$. To demonstrate the effect of having constraints on η , Figure B2 compares MCMC results for CPL+XS Mock 35, a highly symmetric cross configuration. The orange contours show the original results while the teal contours show results with the η prior. The prior significantly reduces the phase space volume, but biases in η and h are still present.

We would like to understand how the biases in η and h vary with image configuration. Motivated by the circular double case, we consider the annulus spanned by the images, and we also consider time delays between different pairs of images. We find that the best pre-

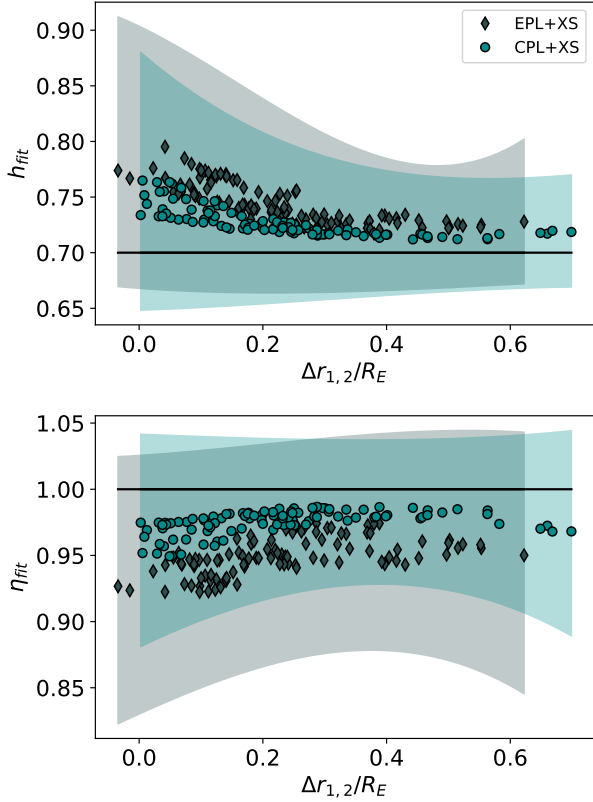


Figure 7. Results for h (top) and η (bottom) values compared to the annulus length normalized by R_E ; points show median values while errorbars show 68% confidence intervals. The CPL+XS case (teal) has less scatter than the EPL+XS case (dark teal). The input truth, $h = 0.7$ and $\eta = 1$, is shown with the black solid line. The shaded errors are interpolated with a univariate spline.

dictors of biases are the time delay ($\tau_{1,2}$) or annulus length ($\Delta r_{1,2}$) between the first and second arriving images. We give preference to the annulus length because it is easily determined from initial observations of a lens. Figure 7 shows the median values and uncertainties for h and η as a function of $\Delta r_{1,2}$ for all of the mock lenses in the CPL+XS case (teal). Overall, h is overestimated and η is underestimated for each system. The bias and uncertainty are larger when the annulus is narrow (e.g., for symmetric configurations like crosses), and they decrease when the annulus is wider (e.g., for short-axis cusps and some folds).

3.3 Quadruply-Imaged Elliptical Power Law + External Shear

Since galaxies can be elliptical, we finally consider the EPL+XS model commonly used in the field. Ellipticity introduces two additional parameters, and this brings the total number of free parameters to nine. To provide enough constraints, we use realistic η and h bounds along with image positions, time delays, and power law slope constraints so that $\chi^2 = \chi_{pos}^2 + \chi_{idel}^2 + \chi_{PL}^2$.

Figure B3 shows MCMC results for EPL+XS Mock 51, a cross configuration. The posterior is still single-peaked but slightly more complicated because there are more free parameters, and there are some covariances (such as between ellipticity and shear, which both describe the angular structure of the lens potential). Bias still exists for this cross configuration, likely due to its lack of constraints on the radial mass profile. Despite using the power law slope as a constraint

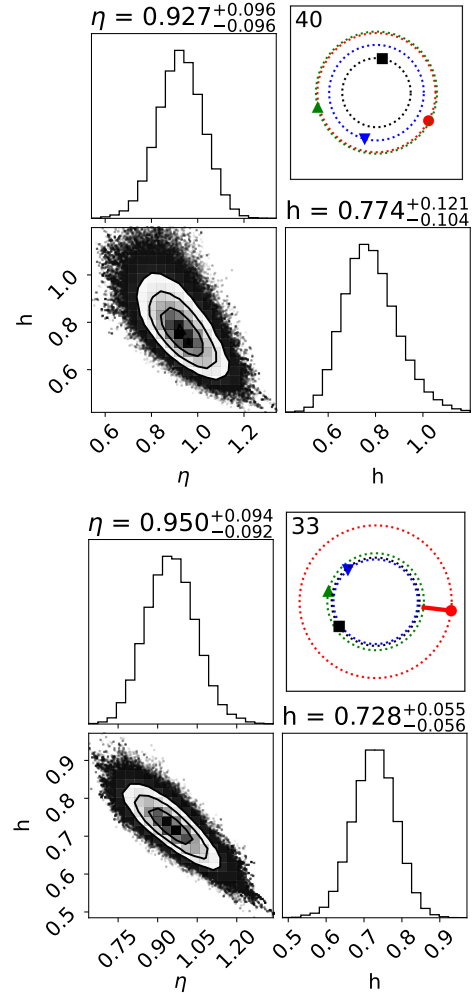


Figure 8. The (η, h) MCMC results for EPL+XS Mock 40 (top) and Mock 33 (bottom), which have the smallest and largest values of $\Delta r_{1,2}$ in the sample, respectively. These two configurations demonstrate the contrast in constraints based on spacing of the first (red circle) and second (green triangle) arriving images. The annulus length $\Delta r_{1,2}$ is indicated with the red solid line.

and having physical ranges for η and h , we find an inaccurate Hubble constant with $h = 0.795^{+0.150}_{-0.127}$.

Results for the full sample of 100 mock EPL+XS quads are shown in Figure 7, and MCMC results for the EPL+XS systems with the smallest (Mock 40) and largest (Mock 33) values of $\Delta r_{1,2}$ are shown in Figure 8. The trends are similar to the CPL+XS case. For both mass cases, fold and short-axis cusp configurations tend to be less biased than crosses and long-axis cusps. However, the EPL+XS biases can be even larger and there is more scatter due to the increased phase volume. The key conceptual result is that the shape of the posterior distribution leads to biases in η and h for all of the types of systems we have considered, and the biases are larger when the image annulus is narrower.

3.4 Combining Probability Distributions for the Hubble Constant

We now consider joint constraints on h from each ensemble of mock lenses. Given the relation between h bias and annulus length in Figure 7, we remove more biased systems by imposing a cut based on the

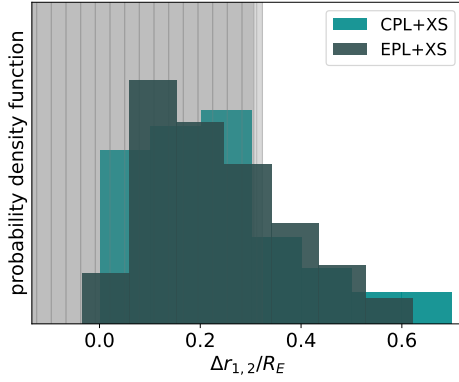


Figure 9. Histograms show the distribution of $\Delta r_{1,2}/R_E$ (image annulus widths normalized by the Einstein radius) for the CPL+XS mock lenses (teal) and the EPL+XS mock lenses (dark teal). The shaded grey region shows the cutoff at $\Delta r_{1,2}/R_E = 0.307$ for CPL+XS and 0.323 for EPL+XS.

annulus length. Such a cut can be replicated in real lens samples since the annulus length is directly observed. Since the bias decreases as annulus length increases, we restrict attention to 25 systems with the highest annulus length. Figure 9 shows the cuts for the CPL+XS and EPL+XS systems compared to the annulus length distribution, where 25 of 100 systems remain for each mass case. Although this selection excludes a majority of the original sample, the number of systems is comparable to what has been used in time delay studies to date. For LSST studies, taking 25% of the full sample will still yield a large ensemble, and will likely be necessary in order to collect all of the ancillary data needed to enable detailed modelling.

For each mock lens, we convert the samples from MCMC into a probability density function using Gaussian kernel density estimation. We treat the mock lenses as statistically independent from each other, so we can combine results by multiplying the probability densities. The overall bias is calculated using the median of the combined distribution, and errors are reported as the 68% confidence interval. Using all systems for the most likely h results in $h = 0.713 \pm 0.007$ (1.86% bias) for CPL+XS and $h = 0.730 \pm 0.008$ (4.22% bias) for EPL+XS. Figure 10 shows how the annulus length cut can reduce the bias to $h = 0.711 \pm 0.011$ (1.62% bias) for CPL+XS and $h = 0.722 \pm 0.012$ (3.20% bias) for EPL+XS.

3.5 Adding Noise

We consider what happens if noise is introduced to the image positions, and then to the image positions and time delays. The original EPL+XS sample gets noise randomly drawn from Gaussians with standard deviations of $\sigma_{pos} = 0.003$ arcsec and $\sigma_T = 2.0$ d. Perturbing by Gaussian noise not only increases the uncertainties, but can also alter the time delay order between images. Figure 11 shows the medians and uncertainties for h and η with the image position noise (red), then the image position and time delay noise (orange). The noise introduces scatter that somewhat obscures the trend with image annulus, but the biases in η and h are still apparent. If all 100 EPL+XS systems are combined, we find $h = 0.735 \pm 0.008$ (4.95%) for image position noise and $h = 0.727 \pm 0.008$ (3.88%) for both image position and time delay noise. Figure 12 shows that selecting systems with the 25 highest $\Delta r_{1,2}$ values results in $h = 0.734 \pm 0.012$ (4.83%) for image position noise and $h = 0.724 \pm 0.012$ (3.40%) for both image position and time delay noise. For comparison, if we select *random* subsamples of 25 systems, the percent bias ranges from

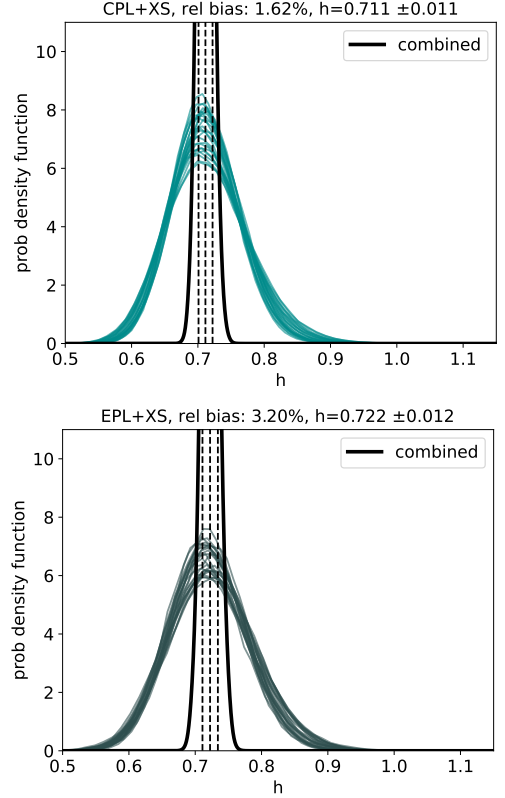


Figure 10. After cutting the data by image annulus, we show the probability densities for h given the information from each mock lens system (colored curves) and the overall probability density for h using all the systems plotted in each panel (black curves). (*top*) The CPL+XS lenses exhibit a relative bias of only 1.62%, while (*bottom*) the EPL+XS lenses exhibit more relative bias of 3.20%.

3-7% for image position noise and 2-9% for both image position and time delay noise. We conclude that selecting by annulus length still tends to reduce the bias in h and η even though measurement noise tends to wash out the trend with image annulus to some degree.

3.6 Comparing Different Time Delay Errors

From Figure 7, it is apparent that models with more bias in h also have larger uncertainties; Figure 13 illustrates that relation for the CPL+XS models. Like the bias itself, the connection between bias and uncertainty arises from the ‘flared’ shape of the posterior distribution for η and h . In our final test, we double the time delay uncertainties to 4 days (using the same source positions and image configurations as before). Figure 13 shows that having larger time delay uncertainties increases the bias and uncertainty for h but has little effect on η . Conceptually, the power law slope η is mainly determined by the image positions, while h is sensitive to the time delays.

4 CONCLUSIONS

Many studies of H_0 bias with lensing focus on how discrepancies between the fitted and intrinsic lens mass distributions lead to bias. We have found that even while using the *same* model to generate and fit lens galaxies, a statistical bias can occur at the level of 3-5%,

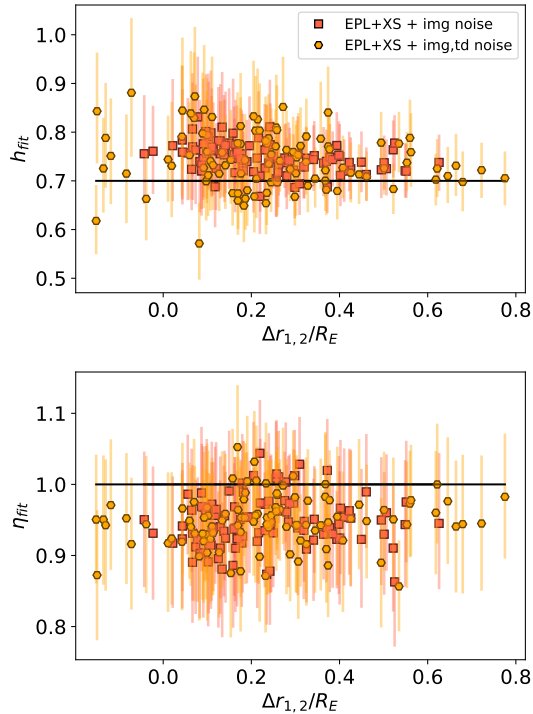


Figure 11. Similar to Figure 7, but now including noise first in the image positions alone (red), and then image positions and time delays (orange). Some annulus lengths shift due to the image position noise and new time delay order in some cases.

depending on whether the elliptical lenses have noise or not. The bias is a consequence of the shape of the posterior distribution. The radial profile degeneracy creates a covariance between h and the power law slope η , and the posterior broadens as h increases and η decreases, so there is more phase space at higher h and lower η . We summarize our key conclusions as follows:

- This statistical bias occurs even in a simple mass distribution like the CPL without shear (Fig. 3). When the image annulus is narrow, the images do not provide enough information to constrain the radial mass profile, and the radial profile degeneracy means that bias and uncertainty in η translate into bias and uncertainty in h .
- For the CPL+XS case, the fitted h and η values from the MCMC fit follow a trend with the relative time delay or annulus length between the first and second images (Fig. 7). For all lens systems, h is consistently overestimated, while η is underestimated. The amount of bias is smaller with greater annulus length.
- The phase space volume expands with more complicated mass models, and there is more scatter in the fitted values for the EPL+XS case (Fig. 7). The max bias is worse for the EPL+XS case (Fig. B3) as compared to the CPL+XS case (Fig. B2).
- The trend with annulus length suggests a way to mitigate the bias. If we select systems with annulus lengths $\Delta r_{1,2} \geq 0.3$ arcsec, we find an overall h bias of 1.62% for the CPL+XS mock lenses, and 3.20% and for the EPL+XS case (Fig. 10). The annulus length selection reduces, but does not eliminate, the bias.
- Measurement noise introduces scatter that somewhat obscures the relation between image annulus and bias, but we still find that selecting systems with large annuli tends to reduce the bias (Fig. 12).
- The bias and uncertainty are correlated with each other. Although higher h bias is associated with higher η bias, the bias and

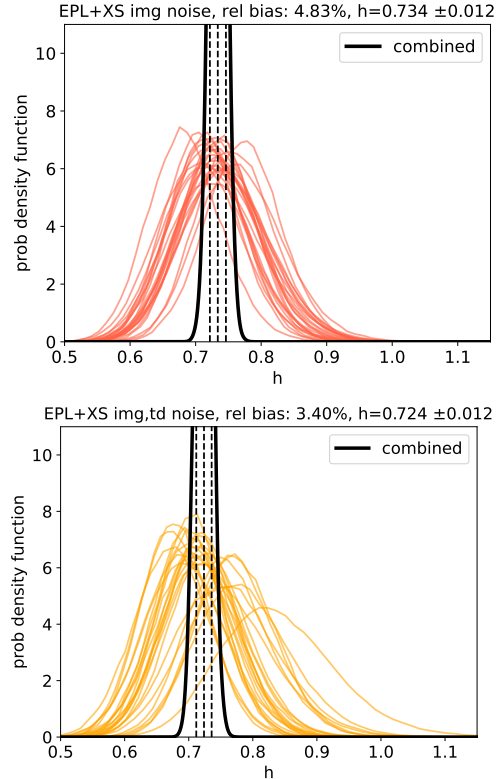


Figure 12. The combined h probability curve for the EPL+XS sample with image position noise (*top*) and image position and time delay noise (*bottom*). Each case uses systems with $\Delta r_{1,2}$ above 0.320 arcsec and 0.357 arcsec, respectively. Although the percent bias is higher with noise, these results are within 1σ of the result in Figure 10.

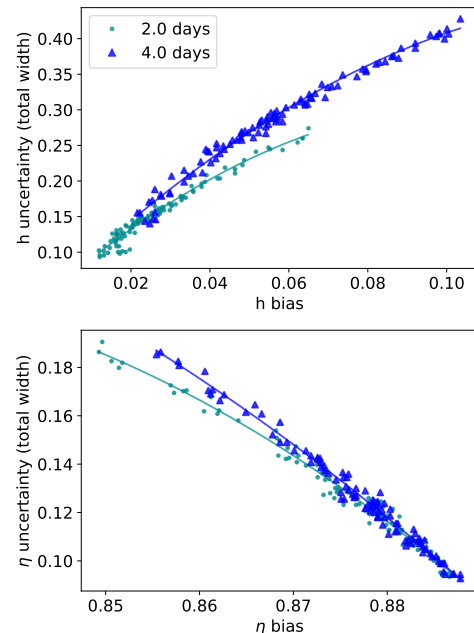


Figure 13. Bias and uncertainty for h (*top*) and η (*bottom*), using CPL+XS models. Teal points show our fiducial results with time delay uncertainties of 2 days, while blue points show results with larger time delay uncertainties of 4 days. The curves show quadratic fits to the points (mainly to guide the eye).

uncertainty for h are more sensitive to time delay errors than for η (Fig. 13).

It is not clear how much this statistical bias might affect current lensing measurements of H_0 . The true mass distribution of lens galaxies are likely to be more complicated than standard lens models, so there may be a mismatch between true and fitted mass distributions that could lead to a systematic bias, different from what we have examined here. Some systems may only have image position and time delay constraints like in our study (Pierel et al. 2023), while other systems also have arcs and stellar kinematics (Sluse et al. 2019; Shajib et al. 2023). Such information can help constrain the radial mass profile in ways that we have not yet explored. Follow-up work should seek to disentangle the effects of the statistical bias we have examined here from systematic biases associated with model mismatch. Follow-up work could also incorporate more observational effects, or different values of ellipticity, shear, and source positions. Selection effects (like the sample being restricted to quads) could contribute to this bias. This would be corrected for in the likelihood function, and would require additional computational effort for efficient MCMC sampling.

In the era of the Hubble tension and large astronomical surveys, lens samples are growing and follow-up observations are often necessary in order to constrain lens models and H_0 with the level of precision necessary to help resolve the Hubble tension. Our results suggest that follow-up observations should prioritize lenses in which the images span wide annuli in order to limit the uncertainties and hence the statistical bias in η and h .

ACKNOWLEDGEMENTS

We thank Simon Birrer, Anowar Shajib, and Alessandro Sonnenfeld for their helpful suggestions. We also thank the Rutgers lensing group: Lana Eid, Somayeh Khakpash, and Aniruddha Madhava for helpful discussions. This work uses the code `pygravlens`, `lensmodel` (Keeton 2011), Python 3 (Van Rossum & Drake 2009), `emcee` (Foreman-Mackey et al. 2013), `numpy` (Harris et al. 2020), `scipy` (Virtanen et al. 2020), and `pandas` (Reback et al. 2022).

DATA AVAILABILITY

The data underlying this article are available in GitHub at <https://github.com/dilyruan/paper-ruan-keeton-2023>.

REFERENCES

- Akhunov T. A., et al., 2017, *MNRAS*, 465, 3607
 Biggs A. D., Browne I. W. A., 2018, *MNRAS*, 476, 5393
 Birrer S., et al., 2020, *A&A*, 643, A165
 Bonvin V., et al., 2018a, *A&A*, 616, A183
 Bonvin V., et al., 2018b, *A&A*, 616, A183
 Bonvin V., et al., 2019, *A&A*, 629, A97
 Burud I., et al., 2000, *ApJ*, 544, 117
 Burud I., et al., 2002, *A&A*, 391, 481
 Cappellari M., et al., 2013, *MNRAS*, 432, 1709
 Chen G. C. F., et al., 2019, *MNRAS*, 490, 1743
 Congdon A. B., Keeton C., 2018, Principles of Gravitational Lensing: Light Deflection as a Probe of Astrophysics and Cosmology. Springer
 Courbin F., et al., 2018, *A&A*, 609, A71
 Di Valentino E., et al., 2021, *Classical and Quantum Gravity*, 38, 153001
 Ding X., et al., 2021, *MNRAS*, 503, 1096
 Eulaers E., et al., 2013, *A&A*, 553, A121
 Falco E. E., Gorenstein M. V., Shapiro I. I., 1985, *ApJ*, 289, L1
 Fassnacht C. D., Xanthopoulos E., Koopmans L. V. E., Rusin D., 2002, *ApJ*, 581, 823
 Foreman-Mackey D., Hogg D. W., Lang D., Goodman J., 2013, *PASP*, 125, 306
 Freedman W. L., 2021a, *ApJ*, 919, 16
 Freedman W. L., 2021b, *ApJ*, 919, 16
 Freedman W. L., et al., 2019, *ApJ*, 882, 34
 Goicoechea L. J., Shalyapin V. N., 2016, *A&A*, 596, A77
 Gomer M., Williams L. L. R., 2020, *J. Cosmology Astropart. Phys.*, 2020, 045
 Hainline L. J., et al., 2013, *ApJ*, 774, 69
 Harris C. R., et al., 2020, *Nature*, 585, 357
 Jakobsson P., Hjorth J., Burud I., Letawe G., Lidman C., Courbin F., 2005, *A&A*, 431, 103
 Keeton C. R., 2011, GRAVLENS: Computational Methods for Gravitational Lensing, Astrophysics Source Code Library, record ascl:1102.003 (ascl:1102.003)
 Knox L., Millea M., 2020, *Phys. Rev. D*, 101, 043533
 Kochanek C. S., 2002, *ApJ*, 578, 25
 Kochanek C. S., 2020, *MNRAS*, 493, 1725
 LSST Dark Energy Science Collaboration 2012, arXiv e-prints, p. arXiv:1211.0310
 Lovell J. E. J., Jauncey D. L., Reynolds J. E., Wieringa M. H., King E. A., Tzioumis A. K., McCulloch P. M., Edwards P. G., 1998, *ApJ*, 508, L51
 McKean J., et al., 2015, in Advancing Astrophysics with the Square Kilometre Array (AASKA14). p. 84 (arXiv:1502.03362), doi:10.22323/1.215.0084
 Millon M., et al., 2020a, *A&A*, 639, A101
 Millon M., et al., 2020b, *A&A*, 640, A105
 Oguri M., Marshall P. J., 2010, *MNRAS*, 405, 2579
 Patnaik A. R., Narasimha D., 2001, *MNRAS*, 326, 1403
 Pesce D. W., et al., 2020, *ApJ*, 891, L1
 Pierel J. D. R., et al., 2023, *ApJ*, 948, 115
 Planck Collaboration et al., 2020a, *A&A*, 641, A6
 Planck Collaboration et al., 2020b, *A&A*, 641, A6
 Poindexter S., Morgan N., Kochanek C. S., Falco E. E., 2007, *ApJ*, 660, 146
 Rathna Kumar S., et al., 2013, *A&A*, 557, A44
 Reback J., et al., 2022, pandas-dev/pandas: Pandas 1.4.2, Zenodo, doi:10.5281/zenodo.6408044
 Reid M. J., Pesce D. W., Riess A. G., 2019, *ApJ*, 886, L27
 Riess A. G., Casertano S., Yuan W., Macri L. M., Scolnic D., 2019, *ApJ*, 876, 85
 Romanowsky A. J., Kochanek C. S., 1999, *ApJ*, 516, 18
 Rusu C. E., et al., 2020, *MNRAS*, 498, 1440
 Saha P., 2000, *AJ*, 120, 1654
 Schmidt T., et al., 2023, *MNRAS*, 518, 1260
 Schneider P., Sluse D., 2013, *A&A*, 559, A37
 Shajib A. J., et al., 2022, arXiv e-prints, p. arXiv:2210.10790
 Shajib A. J., et al., 2023, *A&A*, 673, A9
 Shalyapin V. N., Goicoechea L. J., 2019, *ApJ*, 873, 117
 Sluse D., et al., 2019, *MNRAS*, 490, 613
 Tessore N., Metcalf R. B., 2015, *A&A*, 580, A79
 Tessore N., Metcalf R. B., 2016, *A&A*, 593, C2
 Treu T., Koopmans L. V. E., 2002, *MNRAS*, 337, L6
 Treu T., Marshall P. J., 2016, *A&ARv*, 24, 11
 Treu T., et al., 2018, *MNRAS*, 481, 1041
 Van Rossum G., Drake F. L., 2009, Python 3 Reference Manual. CreateSpace, Scotts Valley, CA
 Virtanen P., et al., 2020, *Nature Methods*, 17, 261
 Vuissoz C., et al., 2007, *A&A*, 464, 845
 Weiner C., Serjeant S., Sedgwick C., 2020, *Research Notes of the American Astronomical Society*, 4, 190
 Wong K. C., et al., 2020, *MNRAS*, 498, 1420
 van de Ven G., Mandelbaum R., Keeton C. R., 2009, *MNRAS*, 398, 607

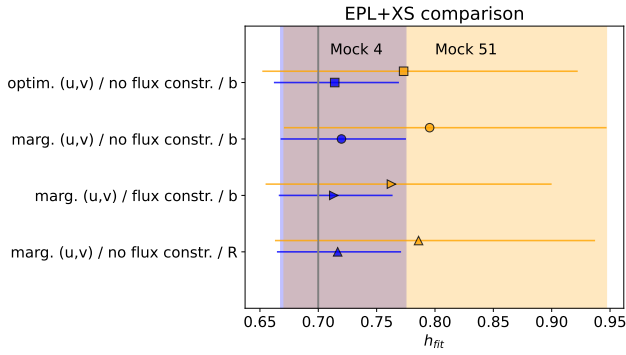


Figure A1. Comparison of the median (markers) and 68% confidence intervals (error bars) for different modelling choices with EPL+XS Mock 4 (blue) and Mock 51 (orange). We consider whether the source coordinates are optimized or fully marginalized (rows 1–2), whether to include flux constraints and optimize the source flux (row 3), and whether to normalize using the ‘R mode’ (row 4). The shaded region shows the ‘control’ mode (row 2) constraints. The vertical grey line shows the true input $h = 0.7$.

APPENDIX A: MODELLING CHOICES

In addition to the mass model, there are other choices that must be made in the modelling process. This work focused on bias with respect to image configurations, and we expect the results to be qualitatively similar if this analysis was performed using a different modelling choice. Still, it is worth quantifying how much these choices affect the results. For illustration, we perform these tests using two mock lenses that exhibit low and high bias with EPL+XS models, namely Mock 4 (a fold configuration) and Mock 51 (a cross configuration). We find that discrepancies between modelling choices is more significant for Mock 51 than for Mock 4. The ‘control’ mode used for the CPL+XS and EPL+XS in this paper is: marginalized source position, no flux constraints, and the Einstein radius parameterized through b .

As described in Section 2.3, our code marginalizes the source coordinates $\beta = (u, v)$ by default. It is computationally simpler to optimize those parameters, so that approach has been adopted in the past (e.g., in `lensmodel`; Keeton 2011). The comparison between source optimization and marginalization for each mock lens is shown in Figure A1, where no flux constraints are used for either case. The h bias is slightly smaller for both mock lenses in the optimization mode. All of the remaining tests use the marginalization mode.

Image flux ratios provide additional constraints on lens models. We add four more constraint terms (for a quad lens) and introduce one more free parameter, namely the source flux, which we optimize. Figure A1 shows that using these constraints reduces h bias and uncertainty for both mock lenses. We omit flux constraints in most of our analysis of quad lenses for simplicity, and since flux constraints are susceptible to microlensing.

As shown in Equations (7)–(10), the lens model can be parameterized using either the Einstein radius R_E (which we call ‘R mode’) or the simple multiplicative factor b (‘b mode’). The two parameters are equivalent for a power law with $\eta = 1$, but for $\eta \neq 1$ they slightly differ and the statistical sampling of the parameter space might also differ. As shown in Figure A1, the ‘R mode’ results are slightly more accurate than the control.

Instead of directly fitting for h , its inverse may be used if one fits for the time delay distance, where $D_{\Delta t} \propto h^{-1}$. We analyze how bias manifests with a h^{-1} parameterization for CPL+XS lenses. We saw overestimated h in the main analysis, and we see a bias for

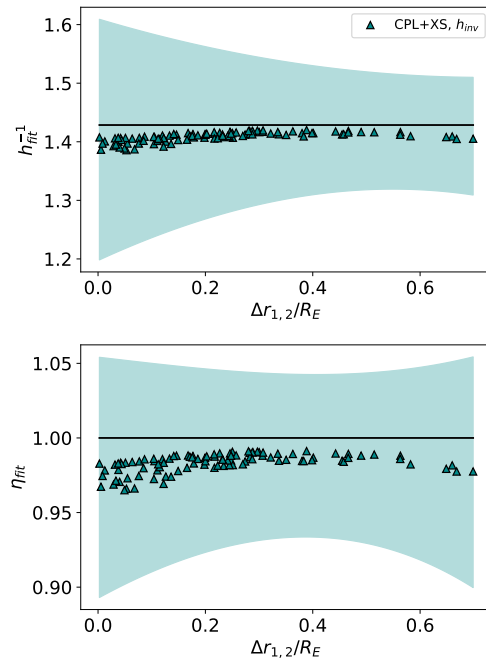


Figure A2. Similar to Figure 7, the bias as a function of normalized annulus length, but with h^{-1} as the free parameter.

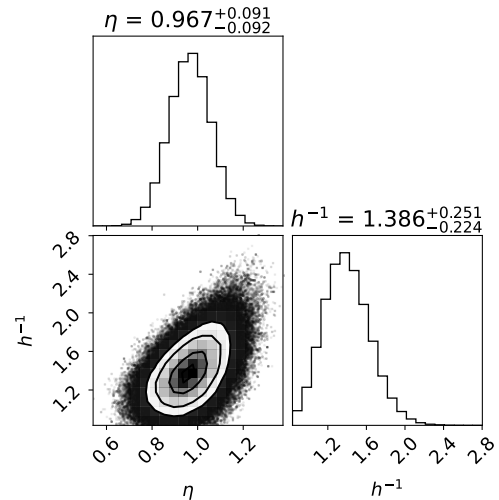


Figure A3. MCMC results for CPL+XS Mock 35, fitting for h^{-1} .

underestimated h^{-1} . Figure A2 shows how both h^{-1} and the mass power law slope are biased low. Figure A3 shows the phase space contours for CPL+XS Mock 35, in contrast to fitting for h in Figure B2.

APPENDIX B: CORNER PLOTS

The full corner plots are shown for a few lenses in Figure B1 (CPL+XS Mock 77), Figure B2 (CPL+XS Mock 35 – with and without the η prior), and Figure B3 (EPL+XS Mock 51).

This paper has been typeset from a \LaTeX file prepared by the author.

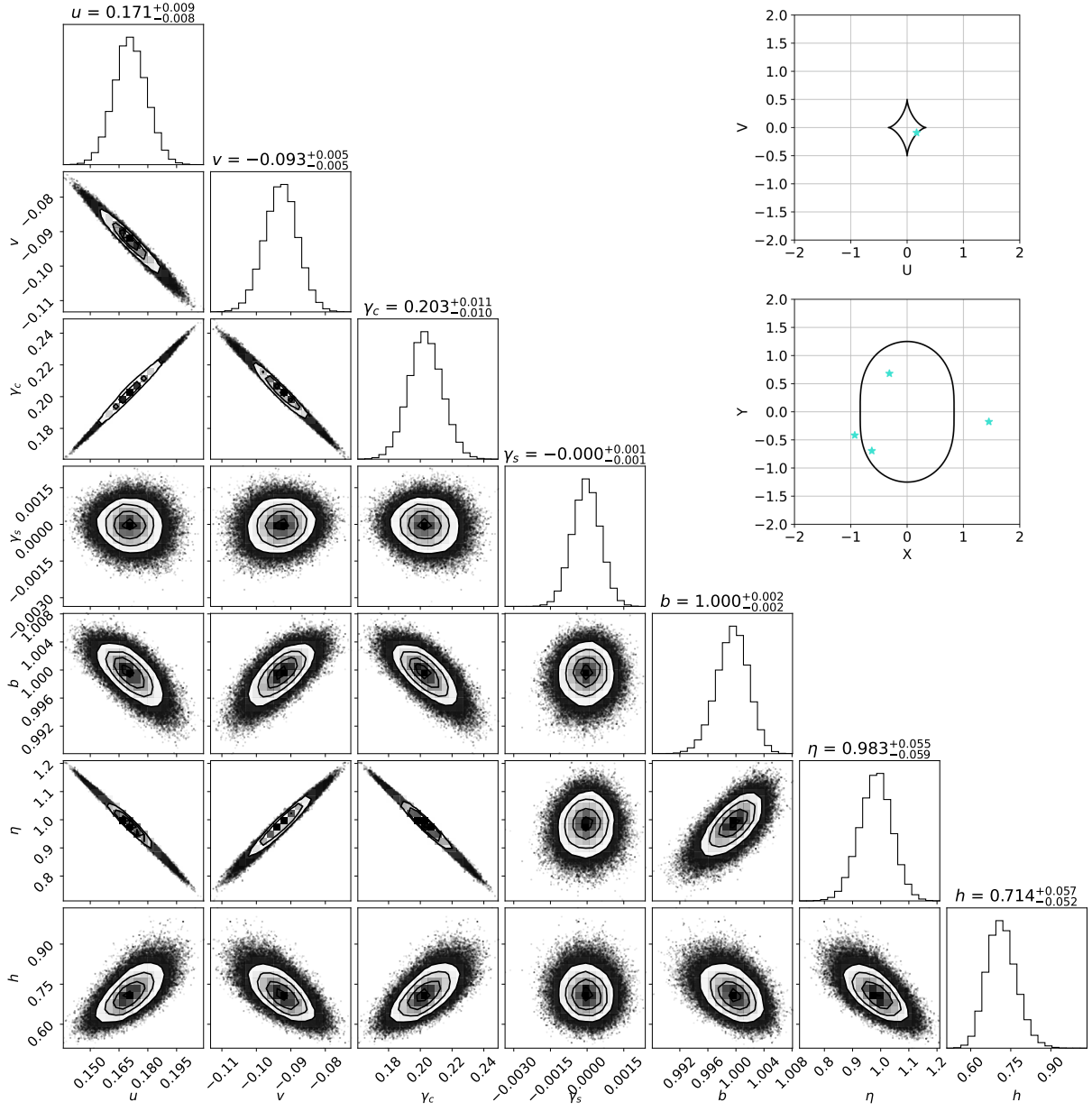


Figure B1. MCMC results for CPL+XS Mock 77. Here u and v represent the source position coordinates, b is the Einstein radius parameter, and γ_c and γ_s are the quasi-Cartesian components of external shear. The posterior distribution is fairly compact and symmetric. There are notable covariances between certain parameters. The upper-right inlay shows the caustics and source position in the source plane (*top*) as well as the critical curves and image positions in the image plane (*bottom*) for this system. Each plane is on an arcsec^2 grid.

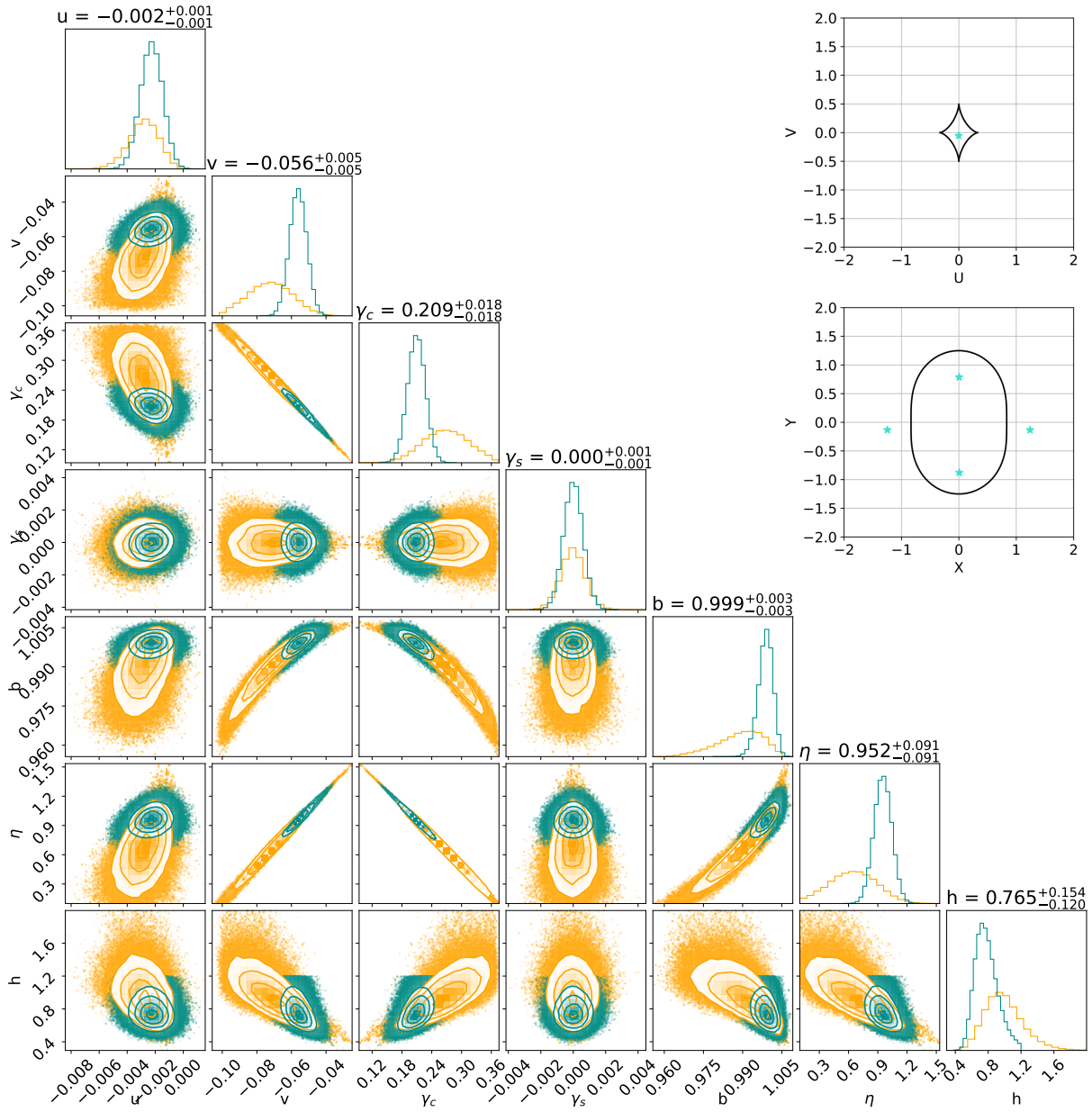


Figure B2. MCMC results for CPL+XS Mock 35, an outlier in the sample. Using only image positions and time delays as constraints (orange), the posterior distribution extends slightly beyond our priors for some parameters, resulting in $\eta = 0.648^{+0.242}_{-0.248}$ and $h = 0.972^{+0.248}_{-0.204}$. This symmetric cross configuration is better constrained (teal and column titles) if we apply constraints on η through the term χ_{PL}^2 in Equation (15). Note: we imposed bounds $\eta \in (0.1, 1.9)$ for the orange case and $\eta \in (0.5, 1.5)$ and $h \in (0, 1.2)$ for the teal case.

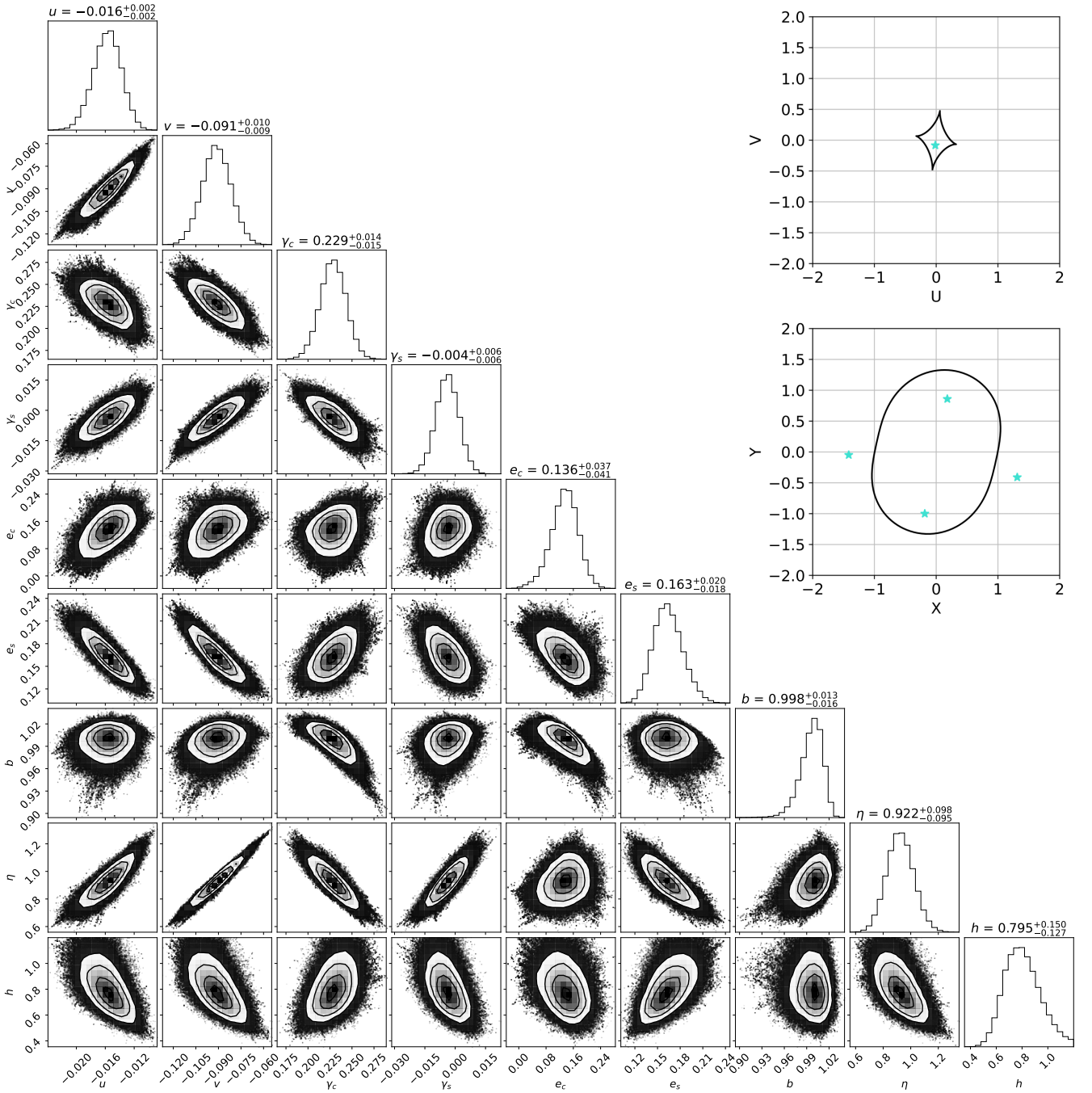


Figure B3. MCMC results for EPL+XS Mock 51. In addition to the fitted parameters in Figure B1, this model includes the quasi-Cartesian ellipticity coordinates e_c and e_s , which makes the phase space contours more complicated than the CPL+XS systems.